Electronic Supplementary Material (ESI) for Lab on a Chip.
This journal is © The Royal Society of Chemistry 2024

Chip-integrated non-mechanical micropump driven by electrowetting on dielectrics

– Electronic Supplementary Information –

Sebastian Bohm,*[a,b,c] Hai Binh Phi,[b,c] Lars Dittrich,[b,c] and Erich Runge[a,b]

1 List of symbols

2 Modelling details
Contact-angle saturation
Interface shape close to the cavity edge
Resistance and inductance values in the equivalent circuit diagram
Gas solubility

3 IR measurements
Fabrication and measurement setup
Tracking algorithm

4 Fabrication - additional information and characterization

5 Supplemental videos

[a] *Technische Universität Ilmenau, Institute of Physics, Group 'Theoretical Physics I', Weimarer Straße 25, 98693 Ilmenau, Germany. E-mail: sebastian.bohm@tu-ilmenau.de*
[b] *Technische Universität Ilmenau, Institute of Micro- and Nanotechnologies, Ehrenbergstraße 29, 98693 Ilmenau, Germany*
[c] *5microns GmbH, Margarethenstraße 6, 98693 Ilmenau, Germany*

1 List of symbols

Symbol	Unit	Explanation
t	s	Time
T	K	Temperature
d_D	m	Thickness of the dielectric layer
γ_{lv}	$N m^{-1}$	Interfacial tension between the liquid and the air
U	V	Applied actuation voltage
ϑ_Y	rad	Young angle at the triple-phase contact line
ϑ	rad	Contact angle at the triple-phase contact line
ε_0	$A s V^{-1} m$	Vacuum permittivity
$\varepsilon_{r,D}$	1	Relative permittivity of the dielectric layer
p_L	Pa	Laplace pressure
p_G	Pa	Vapor pressure of the enclosed gas
p_0	Pa	Applied overpressure at the cavity inlet
p_{at}	Pa	Pressure within an empty cavity
p_{in}	Pa	Pressure at the inlet of a cavity
Δp	Pa	Pressure due to external loads
$V_{C,0}$	m^3	Volume of an empty cavity
ΔV_C	m^3	Volume change of the liquid inside of one single cavity
R_C	m	Radius of a cylindrical cavity
H_C	m	Etch depth of a cavity
S_C	m	Side length of a cavity with a square cross-section
D_H	m	Hydraulic diameter
A	m^2	Cross-sectional area of a cavity
P	m	Wetted circumference of the cavity
τ_{therm}	s	Thermal diffusion time
α_{therm}	$m^2 s^{-1}$	Thermal diffusivity
T	s	Period time
f_0	Hz	Actuation frequency
Re	1	Reynolds number
ρ	$kg m^{-3}$	Density of the liquid
μ	Pa s	Dynamic viscosity of the liquid
L_E	m	Entrance length
$\tau_{unsteady}$	s	Viscous time scale
U_0	V	Amplitude of the actuation voltage
Z_{Ch}	$Pa s m^{-3}$	Fluidic resistance of the pump chamber
L	$Pa s^2 m^{-3}$	Fluidic inductance of the pump
Δp_{Tot}	Pa	Total pressure drop over the pump
Δp_{Circ}	Pa	Total pressure drop over the pump in the equivalent circuit diagram
Δp_T	Pa	Pressure drop over the Tesla valve
$\Delta p_{F/B}$	Pa	Pressure drop over the Tesla valve for the forward and backward direction
$i, \dot{V}$	$m^3 s^{-1}$	Flow rate
$\dot{V}_0$	$m^3 s^{-1}$	Flow rate amplitude
ΔV_C	m^3	Volume change of the liquid inside of each cavity

Symbol	Unit	Explanation
ΔV	m^3	Net pumped volume
N_C	1	Total number of cavities
H_cp	$\mathrm{mol\,atm^{-1}\,l^{-1}}$	Henry solubility constant
D	$\mathrm{m^2\,s^{-1}}$	Diffusion coefficient
w_i	1	Weighting factors
$Z[\gamma_\mathrm{P}]$	1	Objective function in the topological optimization
Di	1	Diodicity of the Tesla valve
ΔE_Disp	1	Ratio of the dissipated energy
A_O	m^2	Area of the design domain
γ_P	1	Material distribution function
F_D	$\mathrm{N\,m^{-3}}$	Darcy force
$\vec{u}_\mathrm{F/B}$	$\mathrm{m\,s^{-1}}$	Flow profiles for the forward and the backward direction
q	1	Convexity parameter
α_max	$\mathrm{Pa\,s\,m^{-2}}$	Porosity parameter
$N_{\dot{V}}$	1	Number of different flow rates
$\dot{V}_\mathrm{max}$	$\mathrm{m^3\,s^{-1}}$	Maximum flow rate
$u_{\mathrm{in},i}$	$\mathrm{m\,s^{-1}}$	Inlet velocities
R_cap	m	Radius of the capillaries
$z_{1/2}$	m	Tracked interface positions
L_cap	m	Total length of the liquid column in the two capillaries
g	$\mathrm{m\,s^{-2}}$	Gravitational acceleration
ϑ_sat	rad	Saturation contact angle
U_sat	V	Saturation voltage
U_T	V	Width of the transition voltage range
ϑ_simu	rad	Contact angle curve including contact angle saturation
R_E	m	Edge rounding radius
R_M	m	Radius of curvature
V_I	m^3	Liquid volume in the region of the rounded edge
V_M	m^3	Liquid volume of the meniscus inside the cavity
N_S	1	Number of stripes
$y_{\mathrm{S},n}$	m	Center position of each stripe
S_n	1	Averaged gray-value curves
f_n	$\mathrm{m^{-2}}$	Time progressions of the second spatial derivatives
$x_{\mathrm{M},n}$	m	Position of the maximum value of the derivatives
$x_{\mathrm{I},n}$	m	Fitted interface position
N_F	1	Fourier order used for the fit
K_n	m	Fitted function describing the shape of the interface

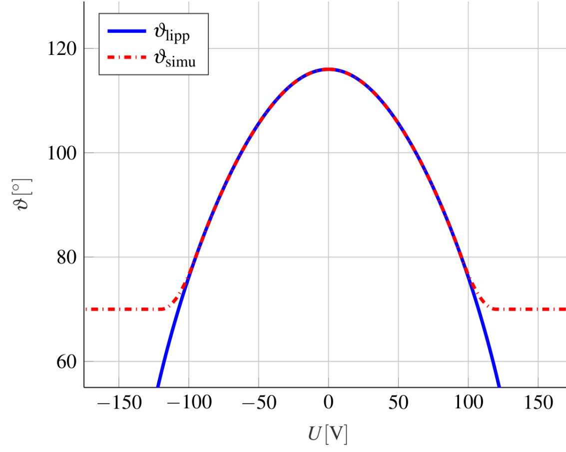

Fig. 1 Contact-angle saturation: The blue line shows the voltage-dependent contact angle according to the Young Lippmann equation. The red dashed line shows the contact-angle curve taking into account contact-angle saturation.

2 Modelling details

2.1 Contact-angle saturation

The Lippmann equation predicts a quadratic decrease in the cosine of the contact angle with an increasing voltage. This behavior is generally observed experimentally for small voltages. However, experiments show that above a certain voltage the contact angle does not decrease any further and instead a constant contact angle value is approached. This phenomenon is known as contact-angle saturation and is not yet fully understood. However, it is crucial for the quantitatively correct description of the wetting behavior at higher voltage values. Here, a phenomenological model is used to account for contact-angle saturation in the simulation of the pump, see Fig. 1. The voltage-dependent contact-angle curve is divided into three regions. We assume a symmetrical curve and, thus, consider only the positive voltage range. Up to a given voltage U_1, the contact-angle curve follows the Young-Lippmann equation:

$$\cos(\vartheta_{\text{lipp}}(U)) = \cos(\vartheta_{\text{Y}}) + \frac{\varepsilon_0 \varepsilon_{\text{r,D}}}{2 d_{\text{D}} \gamma_{\text{lv}}} U^2 \tag{1}$$

Above a second voltage $U_2 > U_1$, the contact angle is assumed to be constant and equal to a value ϑ_{sat}. The voltage difference $U_2 - U_1$ is referred to as U_{T} and the mean value as U_{sat}, i.e. $U_{1,2} = U_{\text{sat}} \mp U_{\text{T}}/2$. We choose U_{sat} to be the voltage where the contact angle evaluated according to the Young-Lippmann equation, i.e. Eq. 1, is equal ϑ_{sat}. The voltage values $U_{1,2}$ are thus determined by specifying the saturation angle ϑ_{sat} and the width of the transition area U_{T}. This means that in addition to the parameters occurring in the Young-Lippmann equation, two further parameters ϑ_{sat} and U_{T} are required for modeling the contact-angle saturation. In the transition range between the two voltages U_1 and U_2, the contact-angle curve is described by a third order polynomial:

$$\vartheta_{\text{simu}}(U) = aU^3 + bU^2 + cU + d \tag{2}$$

The coefficients a, b, c and d are determined by the condition that the contact-angle curve and its derivative are continuous:

$$\vartheta_{\text{simu}}(U_1) = \vartheta_{\text{lipp}}(U_1)\;, \quad \vartheta_{\text{simu}}(U_2) = \vartheta_{\text{sat}}\;, \quad \left.\frac{\mathrm{d}\vartheta_{\text{simu}}(U)}{\mathrm{d}U}\right|_{U=U_1} = m\;, \quad \left.\frac{\mathrm{d}\vartheta_{\text{simu}}(U)}{\mathrm{d}U}\right|_{U=U_2} = 0 \tag{3}$$

where m is given by:

$$m = -\frac{\varepsilon_0 \varepsilon_{\text{r,D}} U_1}{d_{\text{D}} \gamma_{\text{lv}}} \frac{1}{\sqrt{1 - \cos^2\left(\vartheta_{\text{lipp}}(U_1)\right)}} \tag{4}$$

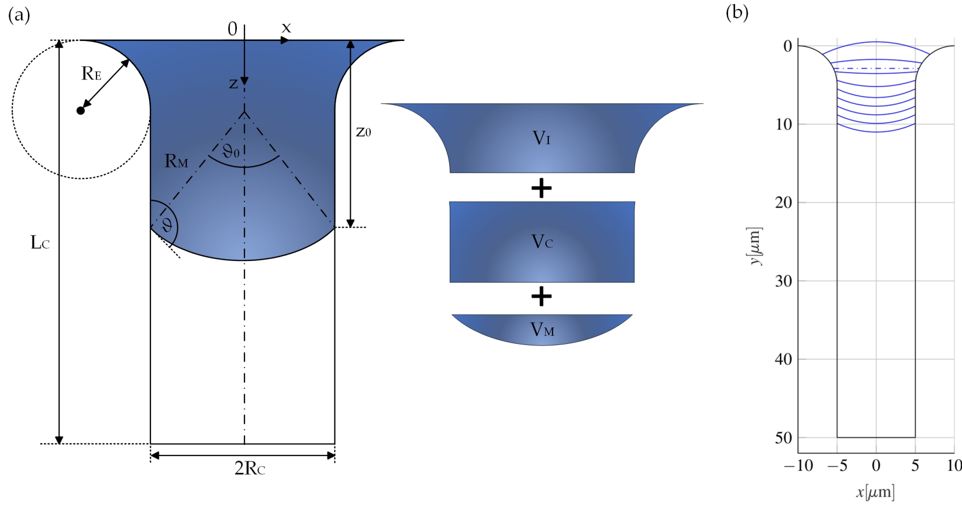

Fig. 2 Modelling of the interface shape close to the cavity edge. (a) Representation of the geometric quantities and the individual volume components. (b) Calculated interface shapes at different volumes for a fixed contact angle $\vartheta = 115°$. The dashed line shows the initial interface shape for $\vartheta_Y = 115°$.

The coefficients result as the solution of the following linear equation system:

$$\begin{pmatrix} U_1^3 & U_1^2 & U_1 & 1 \\ U_2^3 & U_2^2 & U_2 & 1 \\ 3U_1^2 & 2U_1 & 1 & 0 \\ 3U_2^2 & 2U_2 & 1 & 0 \end{pmatrix} \begin{pmatrix} a \\ b \\ c \\ d \end{pmatrix} = \begin{pmatrix} \vartheta_{\text{lipp}}(U_1) \\ \vartheta_{\text{sat}} \\ m \\ 0 \end{pmatrix} \tag{5}$$

An example of the resulting complete voltage-dependent contact-angle curve is shown in Fig. 1.

2.2 Interface shape close to the cavity edge

In order to calculate the pump pressure, the interface shape within the microcavities must be modeled. In the simulation, the Laplace pressure, the gas pressure, and also the interface shape must be known for all values of the volume change ΔV_C and the contact angle ϑ. The edge of the microcavities poses a particular challenge, as it is not clear how the contact angle at a sharp corner should be defined. Therefore, the sharp edge is removed and it is assumed that the edge of the cavities is rounded. The rounding is modeled by a quarter of a circle with a radius R_E. The geometric quantities used are shown in Fig. 2(a). As a result, the Laplace pressure in the region of this rounding is no longer determined solely by the contact angle but also by the liquid volume inside the cavity. For the evaluation of the shape of the interface and the associated pressures, the total volume is divided into three parts as shown in Fig. 2(a). One part corresponds to the volume in the region of the rounded edge of the microcavity with flat interface, shown as V_i in Fig. 2(a). It is given by the volume of the solid of revolution formed by the rounded edge of the cavity:

$$\begin{aligned} V_I(z) =& \pi \int_0^z \left(R_C + R_E - \sqrt{R_E^2 - (x - R_E)^2} \right)^2 \mathrm{d}x = I(x)\Big|_0^z \\ I(x) =& \pi \Bigg((R_C + R_E) R_E^2 \arctan\left(\frac{R_E - x}{\sqrt{2R_E x - x^2}} \right) \\ & - \frac{x^3}{3} + x^2 R_E + x(R_C + R_E)^2 + (R_C + R_E)(R_E - x)\sqrt{2R_E x - x^2} \Bigg) \end{aligned} \tag{6}$$

and the corresponding volume V_{I} is given by:

$$V_{\mathrm{I}}(z_0) = \begin{cases} I(z_0) - I(0) & \text{if } z_0 \leq R_{\mathrm{E}} \\ I(R_{\mathrm{E}}) - I(0) & \text{if } z_0 > R_{\mathrm{E}} \end{cases} \tag{7}$$

The second part of the total volume is formed by the liquid volume V_{C} in the cylindrical region of the cavity. It is given by:

$$V_{\mathrm{C}}(z_0) = \begin{cases} 0 & \text{if } z_0 \leq R_{\mathrm{E}} \\ \pi R_{\mathrm{C}}^2 (z_0 - R_{\mathrm{E}}) & \text{if } z_0 > R_{\mathrm{E}} \end{cases} \tag{8}$$

The remaining part of the volume is given by the volume of the curved meniscus. For the calculation, the radius of curvature R_{M} and the corresponding opening angle ϑ_0 of the spherical segment are calculated. To make the calculations clearer, we first introduce the oriented angle of the surface relative to the 'vertical' z-axis:

$$\beta(z_0) = \begin{cases} \arcsin\left(\frac{R_{\mathrm{E}} - z_0}{R_{\mathrm{E}}}\right) & \text{if } z_0 \leq R_{\mathrm{E}} \\ 0 & \text{if } z_0 > R_{\mathrm{E}} \end{cases} \tag{9}$$

With this, the liquid starts at the cavity surface with the following (oriented) angle:

$$\vartheta_0(z_0) = \vartheta - \beta - \frac{\pi}{2} \tag{10}$$

The volume of a spherical segment described by an angle ϑ_0 and the radius

$$R_{\mathrm{M}}(z_0, \vartheta) = \frac{1}{\sin(\vartheta_0)} \begin{cases} R_{\mathrm{C}} + R_{\mathrm{E}} - \sqrt{2R_{\mathrm{E}} z_0 - z_0^2} & \text{if } \beta \neq 0 \\ R_{\mathrm{C}} & \text{if } \beta = 0 \end{cases} \tag{11}$$

is given by:

$$V_{\mathrm{M}}(z_0, \vartheta) = \frac{\pi}{3} R_{\mathrm{M}}(z_0, \vartheta)^3 \left(2 + \cos(\vartheta_0)\right)\left(1 - \cos(\vartheta_0)\right)^2 \tag{12}$$

We note explicitly that V_{M} and R_{M} are negative for negative ϑ_0. The expression of Eq. 12 is valid even in the – practically irrelevant – case that the air forms a kind of bubble that bulges into the liquid, i.e. for $\vartheta_0 > \pi/2$. The total liquid volume V_{L} in the cavity is thus given for each value of z_0 and ϑ by:

$$V_{\mathrm{L}}(z_0, \vartheta) = V_{\mathrm{I}}(z_0) + V_{\mathrm{C}}(z_0) + V_{\mathrm{M}}(z_0, \vartheta) \tag{13}$$

In the simulation, the time-dependent volume change $\Delta V_{\mathrm{C}}(t)$ in each microcavity results from the integration of the sum of the flow rates divided by the total number of cavities N_{C}, i.e. $\Delta V_{\mathrm{C}}(t) = \frac{1}{N_{\mathrm{C}}} \int_0^t \left(\dot{V}_1(t') + \dot{V}_2(t')\right) \mathrm{d}t'$. To calculate the associated deflection z_0, i.e. $z_0(t) = z_0(V_{\mathrm{C}}(t))$, the optimization problem:

$$\min_{z_0(t) \in \mathbb{R}} F(z_0(t)) = \left[\Delta V_{\mathrm{C}}(t) - V_{\mathrm{L}}(z_0(t), \vartheta(t))\right]^2 \tag{14}$$

is solved, where the contact angle $\vartheta(t)$ is solely determined by the value of the applied voltage $U(t)$ by the equations derived in subsection 2.1, i.e., $\vartheta(t) = \vartheta_{\mathrm{simu}}(U(t))$. Once the deflection z_0 for the actual value of the volume change ΔV_{C} is known, the associated Laplace pressure p_{L} can be determined using:

$$p_{\mathrm{L}}(z_0, \vartheta) = \frac{2\gamma_{\mathrm{lv}}}{R_{\mathrm{M}}(z_0, \vartheta)} \tag{15}$$

The change in the gas pressure inside the cavity is given by:

$$\Delta p_{\mathrm{G}}(\Delta V_{\mathrm{C}}) = \frac{p_0 V_0}{V_0 - \Delta V_{\mathrm{C}}} - p_0 \tag{16}$$

where V_0 corresponds to the gas volume inside the cavity that remains after the initial interface shape has been reached. It is assumed that without applying a voltage or an additional overpressure, the interface is formed in such a way that it is flat and forms the contact angle ϑ_Y, i.e. Young's

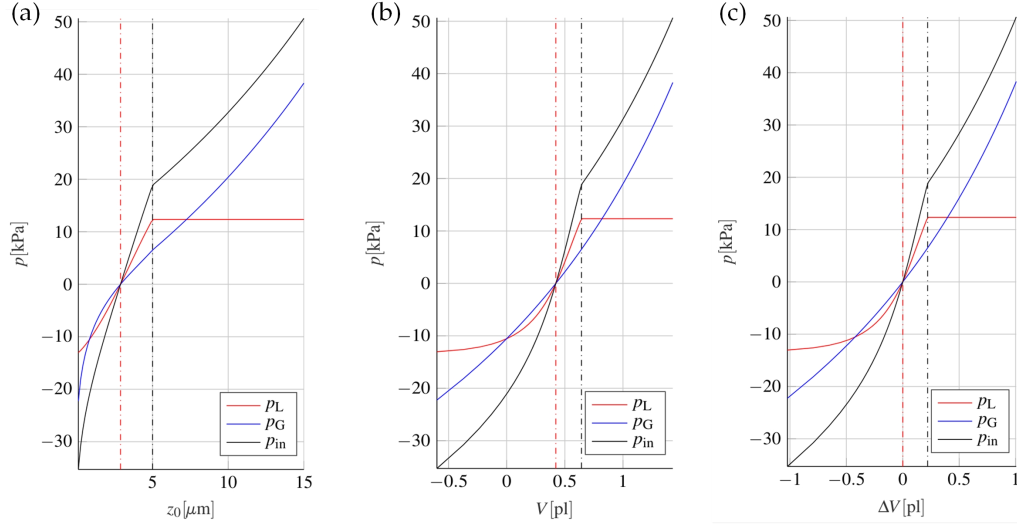

Fig. 3 Calculated pressure curves as a function of (a) the interface deflection z_0, (b) the liquid volume V_L inside the cavity, and (c) the total volume change. In each case, the dashed red line indicates the initial interface state, i.e. the interface shape with a vanishing pressure. The black dashed line marks the filling level where the interface enters the cylindrical region of the cavity and the Laplace pressure becomes constant.

angle, with the cavity edge. The corresponding value of the initial deflection $z_{0,i}$ is given by:

$$z_{0,i} = R_E - \sqrt{R_E^2 - \sin^2(\vartheta_Y - \pi)\, R_E^2} \tag{17}$$

and the corresponding volume V_0 can be calculated via:

$$V_0 = V_I(z_{0,i}) \tag{18}$$

Knowing the Laplace pressure and the gas pressure for the actual volume change, the total pressure p_{in} can finally be calculated using:

$$p_{in}(\Delta V_C, \vartheta) = \Delta p_G(\Delta V_C) + p_L(z_0(\Delta V_C), \vartheta) \tag{19}$$

which is then used for the numerical solution of the differential system of equations. Examples of the resulting interface shapes for different filling levels are shown in Fig. 2(b). In addition, examples of the resulting pressure curves are shown in Figures 3(a-c). It should be noted that the equations for the Laplace pressure reduce to equation (4) given in the main document if the interface deflection $z_0(t)$ is greater than the radius of curvature R_E, i.e. the interface is below the curved region. This state is usually reached quickly, as the inertia of the liquid in the pump chamber prevents a complete return to the initial state during actuation. This means that the interface usually oscillates outside the curved region. For this reason, the model presented here is generally only a minor correction to the model shown in the main document. However, the extension presented here results in a model that can be used to get the pressures for all combinations of ΔV_C and ϑ.

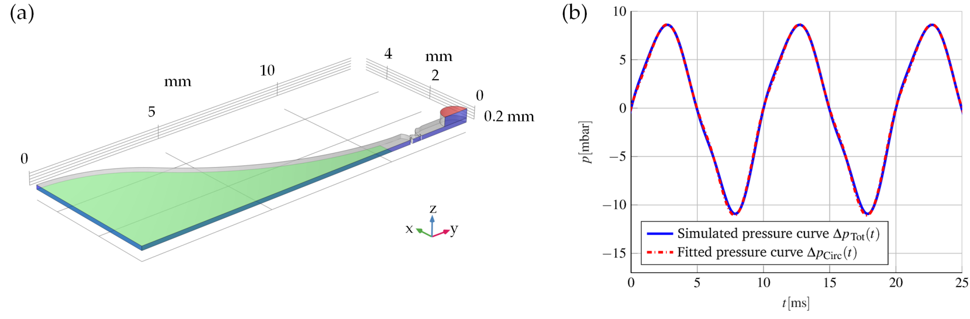

Fig. 4 (a) Three-dimensional model of the micropump that is used for the fluidic simulation in COMSOL Multiphysics. The flow rate is specified on the green face and a constant pressure is imposed on the red surface. A symmetry boundary condition is imposed on all blue faces. It is therefore sufficient to simulate only a quarter of the total geometry. (b) The solid blue line shows the simulated total pressure drop over the pump chamber and the Tesla valve. The red dashed line shows the resulting pressure curve $\Delta p_{\mathrm{Circ}}(t)$ after the optimization of the parameters Z_{Ch} and L. The determined values of the parameters are $Z_{\mathrm{Ch}} = 10.8\,\mathrm{Pa\,s}\mu\mathrm{l}^{-1}$ and $L = 0.0678\,\mathrm{Pa\,s}^2\mu\mathrm{l}^{-1}$.

2.3 Resistance and inductance values in the equivalent circuit diagram

As described in the main document, the parameters Z_{Ch} and L are determined by solving the optimization problem:

$$\min_{Z_{\mathrm{Ch}},L} f(Z_{\mathrm{Ch}},L) = \int_0^{t_e} \left[\Delta p_{\mathrm{Tot}}(t) - \Delta p_{\mathrm{Circ}}(t)\right]^2 \mathrm{d}t \tag{20}$$

$$= \int_0^{t_e} \left[\Delta p_{\mathrm{Tot}}(t) - \left(\Delta p_{\mathrm{T}}(i(t)) + Z_{\mathrm{Ch}} i(t) + L\frac{\mathrm{d}i(t)}{\mathrm{d}t}\right)\right]^2 \mathrm{d}t$$

The total time-dependent pressure drop $\Delta p_{\mathrm{Tot}}(t)$ over the pump chamber and the Tesla valve is determined with the help of a time-resolved fluid flow simulation using COMSOL Multiphysics. The geometry used for the simulation is shown in Fig. 4(a). The solution of Eq. 20 provides values for Z_{Ch} and L that approximate the non-linear pressure curve $\Delta p_{\mathrm{Tot}}(t)$ as well as possible using the equivalent circuit model. This pressure difference is determined by the geometry of the pump chamber and the valve, as well as by the properties of the liquid, specifically its density and viscosity. In addition to the time-resolved flow simulation to determine $\Delta p_{\mathrm{Tot}}(t)$, a steady-state fluidic simulation is carried for different flow rates and the pressure differences $\Delta p_{\mathrm{T}}(i(t))$ across the Tesla valve are determined for both flow directions. The resulting pressure curve is shown in Fig. 5(b) of the main document. The advantage is that only two comparatively inexpensive fluidic simulations are required to determine $\Delta p_{\mathrm{Tot}}(t)$ and $\Delta p_{\mathrm{T}}(i(t))$. From these simulations, parameters Z_{Ch} and L can be determined. Subsequently, the pressure drop can be calculated for arbitrary flow rates and time progressions of the inlet pressure. This makes it easy to vary the number or geometry of the microcavities without the need for additional fluidic simulations. Figure 4(b) shows the simulated time resolved pressure curve $\Delta p_{\mathrm{Tot}}(t)$ together with the resulting pressure curve of the equivalent circuit diagram $\Delta p_{\mathrm{Circ}}(t)$ using the determined values of the parameters Z_{Ch} and L. A sinusoidal flow rate $i(t) = \dot{V}_0 \sin(2\pi f_0 t)$ with an amplitude of $\dot{V}_0 = 5\mu\mathrm{l\,s}^{-1}$ and a frequency of $f_0 = 100\,\mathrm{Hz}$ was specified at the inlet and the resulting pressure drops where calculated. It is evident that the simplified equivalent circuit diagram is sufficiently accurate to describe the pressure drop across the pump chamber and the Tesla valve. The non-linearity in the pressure curves is caused by the non-linear pressure flow resistance $\Delta p_{\mathrm{T}}(i(t))$ of the Tesla valve and the asymmetry of the pressure curve reflects the diodicity of the valve. The small value for $Z_{\mathrm{Ch}} = 10.8\,\mathrm{Pa\,s}\mu\mathrm{l}^{-1}$ means that the flow resistance is mainly caused by the Tesla valve, as desired.

2.4 Gas solubility

We did not include the possibility that parts of the gas enclosed in the microcavities gets dissolved during operation in our modeling. This short section presents some simple estimates to assess the magnitude and relevance of this effect.
The solubility of the trapped gas in the liquid to be pumped can be described with Henry's Law. Typically, the cavities are filled with air before the pump chamber is filled. For simplicity, the enclosed air is described as a mixture of 21% oxygen and 79% nitrogen. It is assumed that the water filled into the pump is initially saturated with air. The corresponding solubility constants are $H_{cp,O_2} = 1.3 \times 10^{-3}\,\mathrm{mol\,atm^{-1}\,l^{-1}}$ for oxygen and $H_{cp,N_2} = 6.1 \times 10^{-4}\,\mathrm{mol\,atm^{-1}\,l^{-1}}$ for nitrogen at a temperature of $T = 298.15\,\mathrm{K}$ [1]. As a result, approx. 23 mg of air can be dissolved in one milliliter of water at a pressure change of one atmosphere. This corresponds to a volume of approx. $19\,\mu$l of air at standard pressure and standard temperature. Thus, at the maximum pump pressure of approx. 15 mbar present in the micropump, an air volume of approx. $0.29\,\mu$l could be dissolved in one milliliter of water. This corresponds to the volume of approx. 55 000 cavities with a side length $S_C = 2R_C = 7\,\mu$m and an etching depth of $H_C = 100\,\mu$m. Thus, the enclosed air of approx. 10% of all cavities in the pump design presented can be dissolved in one milliliter of water, if the maximum pressure of the pump would be present all the time. In many microfluidic systems, however, the total volume of fluid is small. In the experiments presented in Section 3, the total liquid volume is only about $100\,\mu$l. This means that a maximum of only approx. 1% of the gas volume enclosed in all cavities can be dissolved. In such cases, where the total liquid volume in the system is relatively small, the solubility of the enclosed gas can therefore be neglected. However, if a liquid is pumped continuously over a long period of time, the pump performance may decrease due to the solubility of the gas. Furthermore, the presented estimates dramatically overestimate the dissolved gas because it (i) neglects the finite time needed to reach the equilibrium described by Henry's law and (ii) neglects the variation of the pressure varies within each pumping cycle. During every cycle, a phase of compression is followed by a phase of expansion. Due to the slow diffusion of air in water with a diffusion coefficient of $D \approx 0.002\,\mathrm{mm^2\,s^{-1}}$ (cf. Cussler [2]) a region of increased air concentration will form near the liquid-air interface in each microcavity. For this reason, the concentration difference decreases and thus, also the solubility of the gas. In addition, during the expansion phase of each pump cycle, some of the dissolved air in the liquid will be released back into the microcavity and the decrease in volume of the gas will be significantly lower compared to the estimate presented above. As the interface moves further into the microcavity, the gas diffusion is additionally hindered by the cavity walls. As a result, the liquid inside the microcavity close to the interface is practically saturated with air. Thus, the solubility of the enclosed air is to some extent self-limiting. Finally, when the pump chamber is drained, dried and refilled, the initial conditions are restored. In summary, the issue of gas solubility can be ignored for applications where small quantities of liquid are present in the system. However, if a liquid is pumped continuously over a long period of time, the pump performance may decrease due to the solubility of the enclosed air. The modeling via equivalent circuit diagrams described in Subsection 2.3 of the main paper allows to adjust operational parameters when device parameters change over time.

3 IR measurements

3.1 Fabrication and measurement setup

As described in the main paper, a novel method for direct observation of voltage-controlled interfacial motion within individual microcavities using infrared microscopy has been developed. A schematic representation of the respective measurement setup is shown in Fig. 5(a). An infrared microscope is used to look vertically at the chip edge. The chips were manufactured in such a way, that a single row of microcavities is placed near the edge. The edge of the chip is sealed using a microscope slide. The reservoir that forms between the frontside of the chip and the microscope slide is filled with water. When an AC voltage is applied between the liquid and the chip, the liquid moves inside the cavities as discussed previously. Since silicon is transparent in the infrared, the interfacial movement can be monitored with the microscope. This allows the EWOD effect to be observed directly in microcavities!

Remarkably, we can not only directly observe the EWOD effect for the first time in microcavities, but we can also use a setup that largely corresponds to the actual pump chip. The only difference is the doping level of the silicon wafers: Since the transmission in the infrared range drops significantly with increasing doping, weakly-doped wafers need to be used for the IR measurements. However, the weakly doped silicon causes Schottky contacts to form at the silicon-aluminum interface. As a result, a half-wave of the voltage signal is cut off during the measurements. This can be clearly seen in the supplemental videos. However, this effect does not occur in the actual base wafers of the micropump, as the doping concentration is significantly higher and as a result an Ohmic contact behavior between silicon and aluminum is established.

It is important for the measurement that there are no short circuits between the liquid and the chip. This poses a particular challenge directly at the chip edge, as break-outs usually occur when the chips are separated, preventing a perfect sealing. To avoid such electrical short circuits between the liquid and the chip edge, the wafers are separated into individual chips directly after the cavity structures have been etched and before the SiO_2 layer has been generated. Afterwards the chips are thermally oxidized, forming an oxide layer that covers the entire chip surface and thus also the chip edge. The oxide is removed again and regrown to smooth the DRIE scallops as described in the main text. The oxide layer on the back must then be partially removed to enable electrical contacting. In order to properly structure the oxide layer, the chips are positioned face-down on a carrier wafer with etched pits. These pits are etched just deep enough so that the chips only protrude approx. $10\mu m$ from the wafer surface. Subsequently, the carrier wafer and thus also the backside of the chips is laminated with a layer of the dry film resist Ordyl FP415. The Ordyl layer is then structured using standard UV lithography and rectangular openings measuring approx. $0.25\,cm \times 0.5\,cm$ are created on the backside of each chip. The oxide layer is then removed in the area of the openings using a dry etching process on a PlasmaPro 100 RIE from Oxford Instruments. Afterwards, an approx. $200\,nm$ thick layer of aluminum is deposited on the exposed silicon surface. The Ordyl layer is removed using a lift-off process, while simultaneously structuring the aluminum layer. The workflow is summarized in Fig. 5(b).

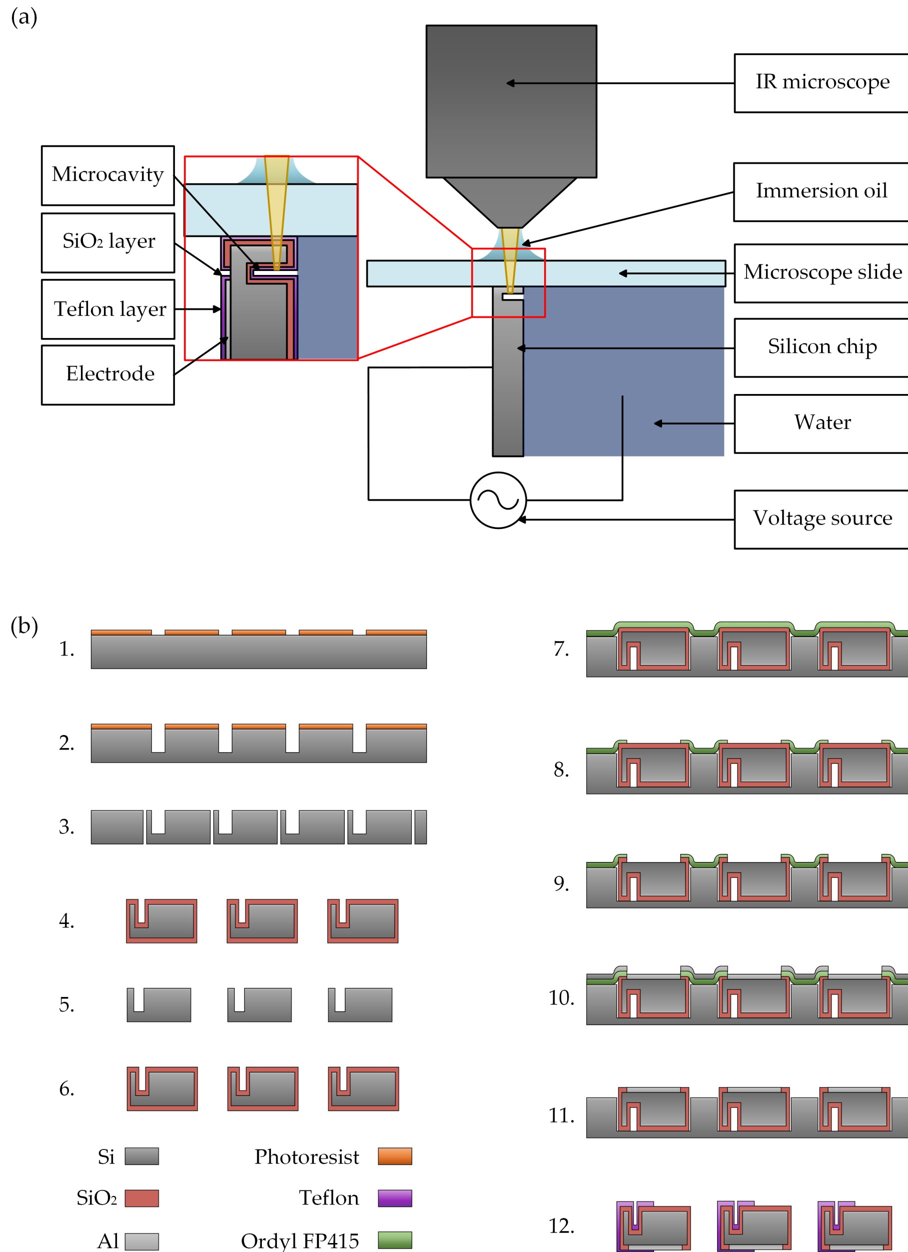

Fig. 5 (a) Schematic representation of the measurement setup used for the infrared measurements. (b) Workflow for the production of IR chips used to demonstrate the pumping effect in individual microcavities. 1. UV Lithography on the front of the wafer to create the microcavities. 2. Transferring the microcavity structures to the silicon wafer using DRIE. 3. Separation of the wafer into individual chips using a dicing process. 4. Growing a layer of SiO_2 on the chip surfaces using thermal oxidation to smooth the DRIE scallops. 5. Wet-chemical removal of the oxide layer using hydrofluoric acid. 6. Renewed thermal oxidation to create the dielectric intermediate layer on the chip surfaces. 7. Lamination of the chip backside with a layer of Ordyl FP415. 8. UV lithography for structuring the Ordyl layer on the back. 9. Opening of the oxide layer on the backside using reactive ion etching. 10. Deposition of a approx. $200\,\mathrm{nm}$ thick aluminium layer on the backside of the base wafer. 11. Lift off the Ordyl layer in order to structure the aluminum layer. 12. Hydrophobization of the individual chips by depositing an approx. $150\,\mathrm{nm}$ thick layer of Teflon using dip coating.

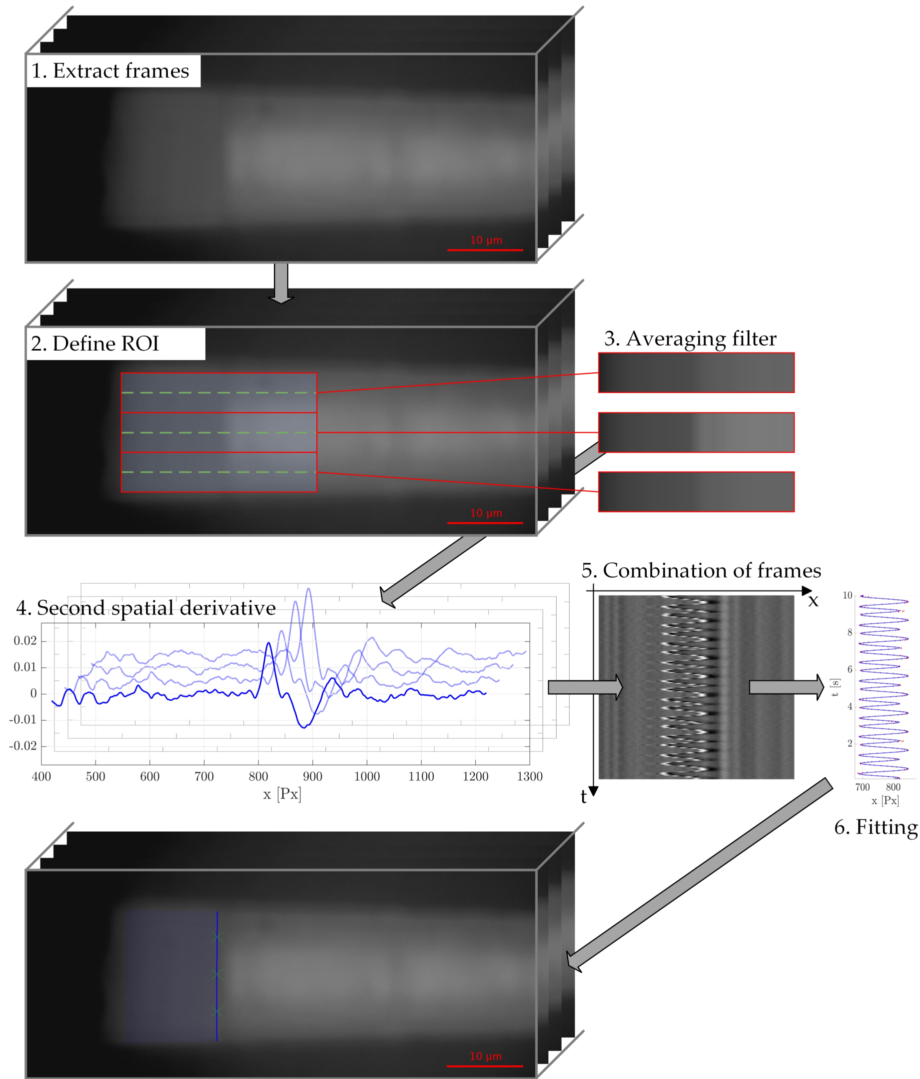

Fig. 6 Schematic representation of the individual steps of the algorithm developed to track the movement of the liquid-air interface in the individual microcavities.

3.2 Tracking algorithm

In order to be able to evaluate the data obtained with the IR-measurement setup described in subsection 3.1, the interfacial movement within the microcavities must be tracked in the videos. This is not an easy task, as the contrast is only caused by the slight differences in reflection due to the different refractive indices of water and air and, thus, usually very low. An in-house multi-stage algorithm is therefore used to reliably track the small differences in contrast. The main steps of the procedure are shown schematically in Fig. 6.

First, the videos are rotated in such a way that the movement of the interface happens parallel to the x-axis. An region of interest (ROI) in which the movement takes place is then defined within the cavity. This ROI is further divided into a predefined number N_S of horizontal strips along the y-axis, with center line $y = y_{S,n}$, $n \in 1,..,N_S$. The number of strips is selected depending on the width of the cavities and is typically between 1 and 4. In each strip and for each frame, the gray values are averaged along the y-axis, yielding averaged gray-value curves $S_n(x)$ along the x-axis. In principle, the interface positions can be defined as the position of the maximum value of the second spatial derivatives, $f_n(x,t) = S_n''(x)$, calculated for the curves $S_n(x)$ for each stripe n and all frames, which are labeled by the respective time t. However, in order to make the analysis numerically more

stable, the maximum positions is not evaluated directly, but instead fitted with a Fourier series: In order to do so, the second spatial derivatives $f_n(x)$ are combined across all frames for each stripe, resulting in time progressions of the derivatives $f_n(x,t)$. For each time point and stripe, the position of the maximum value of the derivatives, i.e.:

$$x_{\mathrm{M},n}(t) = \arg\max_x f_n(x,t) \tag{21}$$

is determined. These values are then fitted with a Fourier series of the form:

$$x_{\mathrm{I},n}(t) = \sum_{n=0}^{N_\mathrm{F}} a_n \cos(n\omega t) + \sum_{n=1}^{N_\mathrm{F}} b_n \sin(n\omega t) \tag{22}$$

Best results are obtained if the order N_F is between 3 and 5. The functions $x_{\mathrm{I},n}(t)$ provide the time-dependent interface position for each strip. The shape of the interface is finally determined by a weighted fit of the points $K_n(t) = (x_{\mathrm{I},n}(t), y_{\mathrm{S},n})$ at each point in time with a polynomial of order $\min(N_\mathrm{S} - 1, 2)$, where the value of the second derivative at the maximum position is used as weighting factor.

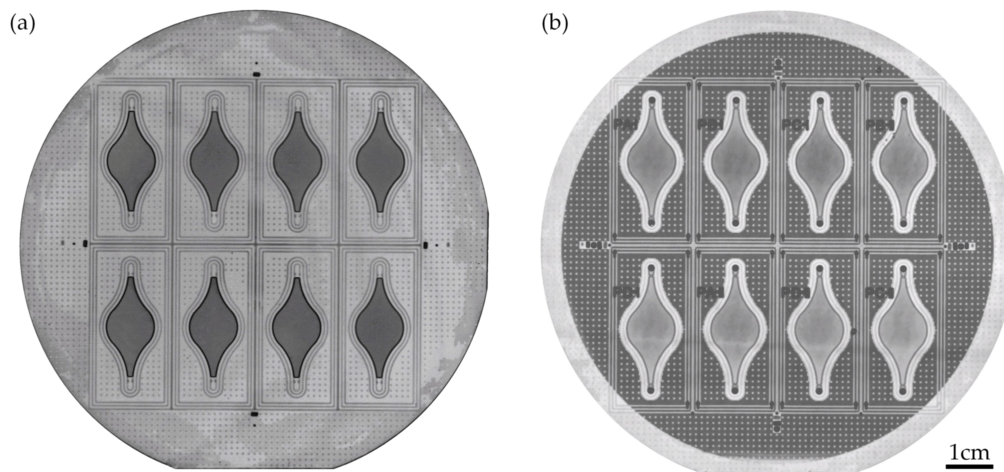

Fig. 7 Scanning Acoustic Microscope images of a fully bonded wafer stack before dicing. (a) The bonding areas surrounding the pump chamber and the individual pump chips made of Ordyl SY330 are clearly visible in the image taken from the backside of the wafer-stack. The microcavities are located in the dark areas. (b) The etched pump chamber, the valve structures, and the fluidic through-holes in the lid wafer can be seen in the image taken from the front side.

4 Fabrication - additional information and characterization

For the micropump to function, the bonding process must be watertight over the entire wafer surface. As the pump is manufactured in silicon, direct visual inspection of the bonding result is not possible. For this reason, the bonding result is checked using Scanning Acoustic Microscopy (SAM). Example images are shown in Fig. 7. It is clear that with the help of the process presented in the main document, an error-free bonding of the two wafers using the Ordyl SY330 takes place over the entire wafer surface.

In addition, the dip-coating process for depositing the Teflon layer was investigated in more detail. For this purpose, the element composition at the cavity surface was examined using Energy-dispersive X-ray (EDX) measurements. The results are summarized in Fig. 8(a-b). This shows in particular the importance of the pre-processing of the SiO_2 surface before the Teflon dip-coating. If the surface is not pre-treated, the adhesion between SiO_2 and Teflon is too poor to achieve a conformal coating of the surface. In contrast, the additional roughness leads to a homogeneous coating of the entire cavity surface as intended.

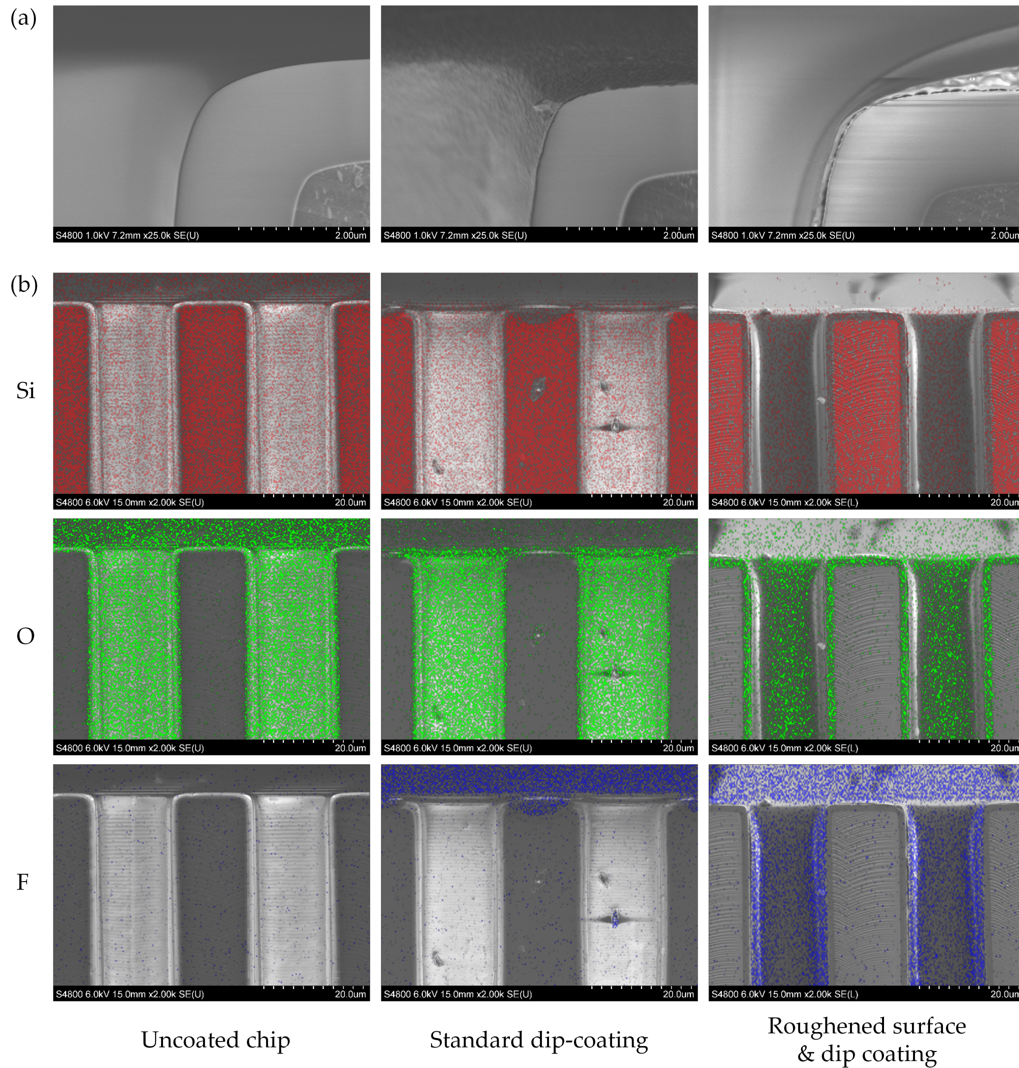

Fig. 8 (a) SEM images of the cleaved edge of a base wafer showing the corner of a single microcavity. Left: Cavity after the oxide layer has been created on the surface. Center: Surface of the microcavity after it has been roughened using HF vapor etching. Right: Cavity after it has been coated with Teflon. The conformal coating of the entire surface and in particular the edge of the cavity becomes clear. (b) Results of the EDX measurements at the cleaved edge of the microcavities after different steps of the processing and different dip-coating methods used for the hydrophobization. The element distribution is superimposed in color over the respective SEM image. In the left column, the element distribution for silicon, oxygen and fluorine are shown for chip before the dip-coating process. No fluorine can be detected. The middle column shows the measurement results after dip coating if the chip surface is not pre-treated. In this case, fluorine can be detected on the surface, but there is no fluorine inside of the cavities. This means that no Teflon coating is present inside of the cavities. In the right column, the measurement results are also shown after dip-coating, but the chip surface was first roughened using an HF vapor etching process and coated with a monolayer of hexamethyldisilazane (HMDS $C_6H_{19}NSi_2$) acting as an adhesion promoter for the Teflon AF solution. In this case, the entire surface is homogeneously coated with Teflon, which is necessary for the micropump to function correctly.

5 Supplemental videos

Three videos are available online showing different measurement results. The content is briefly explained below:

- Pumping action in glass capillaries ("20240111_Pumping_150V_125Hz.mp4")
  This video shows the pumping action in two glass capillaries connected to the pump. For better visualization, the interface in each capillary is tracked with a red arrow outside the capillary. A sinusoidal voltage with a frequency of $f_0 = 125\,\text{Hz}$ and an amplitude $U_0 = 150\,\text{V}$ was used for the actuation.

- EWOD experiments in microcavities ("20240111_IR_Measurements_Cavities.mp4")
  This video shows the time-dependent deflection of liquid-air interfaces within microcavities measured using infrared microscopy. The tracked interface is shown in each case. The cavities have different radii and in addition the deflection is shown at different values of the amplitude of the applied voltage. A frequency of $f_0 = 1\,\text{Hz}$ was used for the actuation. The videos were recorded at 41 fps. It becomes clear that the deflection of the interface increases with a decreasing radius of the cavity and an increasing amplitude of the applied voltage.

- EWOD experiments on droplets ("20240111_EWOD_AC.mp4")
  In this video, an EWOD-activated drop can be seen. The experiments were carried out on flat unstructured chips which are identical in their layer structure to the base wafers. Actuation is performed with a sinusoidal voltage with an amplitude of $U_0 = 100\,\text{V}$ and a frequency of $f_0 = 15\,\text{Hz}$. The extracted contact angles are also shown. A platinum wire with a diameter of approx. 100μm was used to contact the droplet. The droplet has a volume of less than 5μl. The bond number is therefore less than 0.2 and the influence of gravity can be neglected.

References

1 R. Sander, *Atmospheric Chemistry and Physics*, 2023, **23**, 10901–12440.

2 E. L. Cussler, *Cambridge Series in Chemical Engineering: Diffusion: Mass Transfer in Fluid Systems*, Cambridge University Press, Cambridge, England, 2nd edn, 1997.